

Hydro-mechanical behavior of an embankment during inundation

G. M. Rotisciani¹, F. Casini², A. Desideri¹ and G. Sciarra³

Abstract

The paper presents a comprehensive analysis of the hydro-mechanical response of an embankment subject to inundation. The Modified Cam-Clay model extended to unsaturated conditions and formulated in terms of Bishop's effective stress is used to predict the mechanical behavior of the sand-clay mixture. The model's ability to accurately reproduce the embankment response is evaluated by comparing the numerical predictions with the results of the physical model. Time evolution and spatial distribution of the wetting-induced displacements are analyzed together with the stress paths resulting from the imbibition process. The influence of after-compaction conditions on the embankment performance is examined focusing on the occurrence of the volumetric collapse.

Key words: imbibition process, volumetric collapse, partial saturation, constitutive modelling, boundary value problem.

¹ G. M. Rotisciani and A. Desideri, Dipartimento di Ingegneria Strutturale e Geotecnica, Sapienza Università di Roma, Roma, Italia.

² F. Casini, Dipartimento di Ingegneria Civile e Ingegneria Informatica, Università degli Studi di Roma "Tor Vergata", Roma, Italia.

³ G. Sciarra, Dipartimento Ingegneria Chimica Materiali Ambiente, Sapienza Università di Roma, Roma, Italia.

Introduction

Roadway and railway embankments are very common earthworks built by compacting soils, usually in partial saturation regime. The embankments undergo frequent variations in water content due to rainfall events and inundations (Cafaro *et al.* 2008; Tarantino and Pozzato 2008). The resulting variations in saturation degree may cause either elastic swelling or volumetric collapse depending on several factors and, in particular, the initial conditions in terms of void ratio and water content (*e.g.*, from experimental investigations: Lawton *et al.* 1989; Gens *et al.* 1995; Sun *et al.* 2007; Ferber *et al.* 2008; Muñoz-Castelblanco *et al.* 2011; Vilar and Rodrigues 2011; from the theoretical point of view: Alonso *et al.* 1990; Or 1996; Thomas and He 1998; Jommi 2000; Gens *et al.* 2006; Sheng *et al.* 2008; Masin 2010; Casini 2012; Zhou *et al.* 2012). An accurate prediction of wetting-induced deformations is needed to optimize the compaction procedure and, eventually, to limit the displacement field.

The cost of constructing and monitoring full-scale field test embankments, to assess their performance under various imbibition paths, is so expensive as to be impractical. An alternative is to consider reduced scale centrifuge model to analyze the response of embankments compacted with different characteristics during imbibition. Centrifuge modelling, however, has been less commonly used in unsaturated soils (Soranzo *et al.* 2015) compared to dry or saturated soils (see among others Ovesen 1975; Nakase *et al.* 1984; Kimura *et al.* 1985 and White *et al.* 2008).

Thorel *et al.* (2011) conducted a study on a small-scale embankment made of a dry and loosely compacted sand–clay mixture (SCM) using the Laboratoire Central des Ponts et Chaussées (LCPC) geotechnical centrifuge. By comparing the results of the physical modelling with oedometric tests, the Authors aimed to quantify the effect of a low compaction rate on settlement in case of inundation and to assess the relevance of laboratory test-based predictions at the model scale only. They presented the results of

laboratory tests carried out to define the hydro-mechanical properties of the mixture, the outcomes of the centrifuge test and the comparison between measurements and predictions. As oedometric conditions are valid only near the axis of symmetry, Thorel *et al.* (2011) only focused on elements located some distance from the slope.

In this study the test performed by Thorel *et al.* (2011) is back-analysed using the Modified Cam-Clay model (MCCM) extended to unsaturated conditions (Jommi 2000, Tamagnini 2004). The MCCM is formulated in terms of Bishop's effective stress (1959), defined as: $\sigma'_{ij} = \sigma_{ij} - u_a \delta_{ij} + \chi(u_a - u_w) \delta_{ij}$, where σ_{ij} is the total stress, χ coincides with the saturation degree S_r , u_a and u_w are the pore air and pore water pressures, respectively, and δ_{ij} is the Kronecker delta. For sake of simplicity, in the following Bishop's effective stress are briefly indicated as effective stress. The retention behavior is described by the water retention curve (WRC) that relates matrix suction, defined as difference between u_a and u_w , and saturation degree. Differently from the model presented by Tamagnini (2004), the WRC adopted in this work obeys a modified van Genuchten expression, where reversible retention behavior during drying/wetting is assumed. In the numerical simulation, the sequence of steps of the centrifuge test is faithfully reproduced, taking into account the real geometry of the embankment. The main objectives of the study are:

- Validate the extended Modified Cam-Clay model in a real problem;
- Analyze the settlement mechanisms induced by inundation events and the evolution of the more significant hydro-mechanical variables;
- Understand the relevance of the initial conditions on the embankment behavior by performing additional numerical simulations changing the as-compacted conditions.

The study is organized as follows. First, the main features of the centrifuge test are briefly revised. Second, the numerical model is described together with the constitutive

laws used for the fluid and solid phases. Then, the numerical predictions are compared with the measurements in order to validate the MCCM. Once the accuracy and reliability of the numerical results are verified, the hydro-mechanical response of the embankment is analyzed focusing attention on the evolution over time of pore-water pressure, saturation degree and total vertical stress, the stress paths followed by two elements and the displacement field. Finally, the results of two additional numerical analyses are presented to investigate to what extent the embankment response is influenced by dry density and water content.

Centrifuge test

Thorel *et al* (2011) conducted an experimental study on a small-scale embankment made of a sand-clay mixture compacted on the dry side of the optimum Proctor curve. The aim of this study was to evaluate wetting-induced deformations and to assess the relevance of oedometric tests for the prediction of the vertical displacement field near the axis of symmetry. The main features of the centrifuge test are briefly described.

The test is conducted at 100 *g* on a half embankment model 21 cm high made of 40% Speswhite kaolin and 60% Fontainebleau sand. The slope angle is about 33° and the lengths of the base and the crest are 60 and 28.5 cm, respectively. The material used in the test and the geometry of the embankment model are representative for real road embankments. These are commonly built using coarse grained soils mixed with fine particles and the side slopes seldom exceed 1:1 (vertical to horizontal).

The hydro-mechanical properties of the SCM are a combination of those of clayey and sandy soils. The standard Proctor curve is similar to that of fine-grained soils and provides an optimum water content w_{opt} of 13.5% and a maximum dry unit weight γ_{MDD} of 18.7 kN/m³. The compression behavior was investigated by performing a series of oedometric tests (OED) on saturated and unsaturated soil samples. The experimental

data are depicted in the semi-logarithmic compression plane in Fig.1. Because of their low dry density, the saturated samples show a linear relationship between the logarithm of the total vertical stress σ_v and the specific volume v over the entire stress range investigated. Conversely, the unsaturated samples, with a constant water content, present a clear inflection point for σ_v ranging between 400-800 kPa. The observed behavior, in terms of stiffness moduli and values of preconsolidation stress, are qualitatively similar to those expected in the clayey soils. The WRC shown in Fig.2 was obtained using the osmotic method on a soil sample with an initial void ratio e_0 of 0.72.

The embankment model is built inside the strongbox in seven successive sub-layers, each approximately 3 cm thick. The SCM, with a water content w of 10.5%, is compacted on the dry side of the Proctor curve at low compaction rate to emphasize wetting-induced deformations. The after-compaction dry unit weight γ_d is 15.3 kN/m³, corresponding to 82% of γ_{MDD} . A sand layer 2 cm thick is located on the bottom of the strongbox and is surrounded by a geotextile. After deposition and compaction, a portion of the SCM layer is removed to form a slope of 33°. Then, the strongbox is placed in the centrifuge and the gravitational acceleration is quickly increased up to 100 *g* (Phase 1). Once stationary conditions are reached, the strongbox is hydraulically connected to a water tank and the water table is constantly maintained just above the sand-embankment interface level (Phase 2). Finally, the water table inside the main compartment is raised up to 5 cm above the base (Phase 3).

The crest vertical displacements δ_v are recorded by three laser transducers, installed close to the crest slope, and seven regularly spaced LVDTs, installed in the central portion of the embankment top. Soil movements inside the embankment body are monitored by a digital video camera mounted in the centrifuge. By analyzing the images, the settlements of some reference points located at depths ranging from 9 to 18 cm, close to the axis of symmetry, are determined.

Time evolution of the crest vertical displacements are shown in Fig. 3. During the in-flight phase, the settlements increase in magnitude and reach stationary values ranging from 0.6 to 2.4 mm, depending on the distance from the axis of symmetry. In this phase, more extensive vertical displacements are registered near the axis; see data given by LVDT 4. In Phase 2, that takes place 2.6 h after the beginning of the test, the embankment settles again and the variation of δ_v is not significantly affected by the position of the measurement point with respect to the axis. In the last phase, that starts 4.6 h after the beginning of the test, a further increment of the vertical displacements is observed, whose magnitude increases approaching the crest slope.

Thorel et al. (2011) compared the settlements measured in the small scale embankment model close to the axis of symmetry with those predicted on the basis of the oedometric tests. Given the small difference between the final values of δ_v (approximately equal to 10% of the maximum settlement), the Authors concluded that the laboratory tests can be successfully used to determine the order of magnitude of the wetting-induced vertical displacements. Similar results were found by Rodrigues (2007) and Vilar and Rodrigues (2011) analyzing the foundation settlements due to the gradual rise of the groundwater table in the city of Pereira Barreto, Brazil.

Numerical modelling

The hydro-mechanical behavior of the embankment scale model is analyzed by performing plane strain simulations using the commercial code Abaqus/Standard. Three numerical analyses were conducted modifying the after-compaction conditions, as shown in Table 1. The values for w and γ_d assumed in the reference analysis (Test 1) correspond to those measured in the centrifuge test. This simulation was run to validate the MCCM with a set of experimental data and to trace the evolution of the more

significant hydro-mechanical variables, such as suction, saturation degree, specific volume, stress invariants, along an imbibition path. The after-compaction conditions assumed in Tests 2 and 3 are more representative of field conditions in actual road embankments.

After a brief description of the numerical model, the constitutive laws for the fluid and solid phases are presented. Particular attention is paid to the calibration procedure of the constitutive model and the evaluation of its predictive capabilities with reference to elementary soil volumes.

Finite element model

The numerical analyses accurately reproduce the geometry and sequence of steps of the centrifuge test. The soil domain is discretized by a finite element mesh of 88.5 cm in width and 23 cm in height, with element size ranging from (0.5x0.5) cm to (1.0x0.5) cm. The adopted mesh shown in Fig.4 provides stable and accurate solutions that are mostly independent of size effect. The nodes at the lower boundary are constrained by hinges while the nodes located along the lateral sides are free to move vertically. Regarding hydraulic boundary conditions, null water flow is prescribed at all external surfaces.

The interaction between the sand base layer (2 cm thick) and the embankment is modeled as a purely frictional contact with Mohr Coulomb failure criterion.

Under geostatic conditions, because of the small dimensions of the embankment, the total vertical stresses are negligible and the pore-water pressures keep a fairly constant value. To form the slope, the elements located above a surface inclined at 33° to the horizontal plane are removed (Phase 0). Once stationary conditions are reached, the effective stress state is substantially isotropic and coincident with suction scaled by

saturation degree: $\sigma'_v \cong \sigma'_h \cong s S_r$. This result is consistent with the small magnitude of the total stress compared with the suction level.

The g -level is increased instantaneously by a factor of 100 (Phase 1), as in the centrifuge test. Then, null pore water pressure is prescribed at the embankment base to model the rising of the water table (Phase 2). Finally, the inundation event is simulated by imposing a constant pore water pressure of 50 kPa at the sand-embankment interface level and by applying a hydrostatic pore-water pressure distribution on the slope, according to a water table located 5 cm above the base of SCM layer at 100 g (Phase 3).

Constitutive laws for fluid and solid phases

The fluid flow is described by the well-known Richards equation (1931):

$$\nabla \left(\frac{k}{\gamma_w} \nabla (s + \gamma_w z) \right) = \frac{\partial (n S_r)}{\partial t} \quad (1)$$

where γ_w is the specific weight of water, z is the depth, n is the porosity and k is the unsaturated hydraulic permeability defined as: $k = k(S_r) k_{sat}$. $k(S_r)$ is a power function of the degree of saturation: $k(S_r) = S_r^3$ and k_{sat} is the saturated permeability deduced by back-analysing the time evolution of the crest vertical displacements.

The WRC adopted in this study assumes a reversible behavior along drying and wetting paths and neglects the dependency on the current void ratio. The WRC is described by a modified Van Genuchten expression: $S_r = 1/[1 + (\alpha^* s)^l]^m$, where $\alpha^* = \alpha e^{\beta e_0}$. The explicit dependence on the initial void ratio was introduced through α^* in the WRC model to take into account the influence of the initial conditions on retention behaviour. As already stated, the improved model predicts increasing air-entry values as the initial void ratio decreases (e.g. Romero & Vaunat 2000; Salager et al.

2013; Tarantino 2009; Nuth and Laloui 2008). The parameters α , β , l and m are determined by best fitting the experimental data (see Fig.2).

The SCM response along stress paths imposed by oedometric conditions does not qualitatively differ from that of clayey soils as underlined in the previous section. Therefore, the mechanical behaviour can be successfully described using the MCCM extended to the case of partially saturated soils adopting the approach proposed by Jommi and Di Prisco (1994). This model is formulated within the framework of critical state soil mechanics in terms of Bishop's effective stresses.

The main features of the model are reported below; more details on its mathematical formulation can be found in Tamagnini (2004, 2011) and Rotisciani et al. (2015). In this model the yield surface is an ellipse centred on the horizontal axis, expressed as follows:

$$F := q^2 - M^2 p' (p'_c - p') \quad (2)$$

where p' is the mean effective stress defined as: $p' = p + s S_r$; q is the deviator stress correlated to the second invariant of the deviatoric effective stress (J_2): $q = \sqrt{3 J_2}$; M indicates the slope of the Critical State Line (CSL) in the compression triaxial plane; p'_c is the preconsolidation pressure and corresponds to the abscissa of the intersection point between the ellipse and the p' -axis.

The model predicts an isotropic hypoelastic response inside the elastic domain. The evolution laws of the elastic moduli are deduced from the unloading-reloading line (URL) assuming a constant value for Poisson's ratio. Irreversible strains develop when the current stress state reaches the yield surface and the stress increment is oriented outwards with respect to the current elastic domain. The flow rule is associated and the evolution of the yield surface results from a double-hardening mechanism:

$$\dot{p}'_c = \frac{vp'_c}{\lambda - \kappa} \dot{\epsilon}_v^p - bp'_c \dot{S}_r \quad (3)$$

where λ and κ are the slopes of the Normal Consolidation Line (NCL) and the URL in a semi-logarithmic picture of the compressibility plane; b is a constitutive parameter which controls the relative position of the NCL associated with the current S_r with respect to the saturated NCL. The explicit dependence of p'_c from S_r allows to fairly reproduce the increase of the apparent preconsolidation pressure with suction and the collapse upon wetting.

The MCCM is defined knowing six constitutive parameters and three state variables. The constitutive parameters have a clear physical meaning and can be easily determined performing few laboratory tests. These parameters are listed in Table 2 together with saturated permeability and the WRC parameters. The state variables refer to the initial conditions of soil samples and, in particular, to specific volume, saturation degree and preconsolidation pressure.

The MCCM is calibrated with reference to the results of cone penetration tests (CPT) and oedometric tests. CPTs were carried out at 1 g on a "reference" embankment, prepared with the same procedure and the same initial conditions as the centrifuge model. The critical friction angle is deduced from the measurements of the cone penetration resistance using the correlations proposed for saturated soils (Robertson and Campanella 1983; Durgunoglu and Mitchell 1975). The parameters λ and κ are determined directly from the laboratory results as slopes of NCLs and URL in the v - $\ln p'$ plane. N_0 defines the position of the saturated NCL in isotropic conditions on the semi-log compressibility plane and corresponds to the specific volume at $p'=1$ kPa. The value for N_0 is deduced by the oedometric test performed on saturated soil sample, once known λ and κ . The parameter b is evaluated back-analysing the results of OEDs conducted at constant water content and Poisson's ratio ν is assumed equal to 0.25. The

initial conditions, in terms of void ratio and saturation degree, are well defined in all laboratory tests carried out on soil samples and embankment models. The dimension of the yield surface is deduced considering the URL passing through the initial stress state and the NCL related to the initial saturation degree ($v=N(S_r)-\lambda \ln p'$, $N(S_r)= N_0+(\lambda-\kappa) b(1-S_r)$, Casini 2012). The point at the intersection between the two lines identifies the preconsolidation pressure.

The model predictions are compared with the oedometric results in Fig.1 for saturated and unsaturated samples. The comparison highlights the ability of the model to describe the soil behavior along stress paths imposed in 1D compression tests.

Satisfactory results are also obtained by simulating wetting tests performed on soil samples compacted at different dry densities with an initial water content of 10.5%. In these tests the soil is soaked under three constant vertical loadings: 3, 100 and 800 kPa. Figure 5 shows the laboratory results and the numerical predictions in terms of initial (after-compaction)-final (after-inundation) void ratios. Analogously to the experimental results, the model predicts qualitative differences in the soil responses depending on the applied vertical load. Regardless of the after-compaction void ratio, the samples swell when full saturation is reached under a vertical load of 3 kPa. Conversely, reductions in volume due to volumetric collapse phenomena are observed when soil samples are soaked under a vertical load of 800 kPa. Finally, the increase of S_r under a vertical load of 100 kPa entails swelling up to the as-compacted void ratio of 0.5 and positive volumetric deformations with the initial void ratio ranging between 0.5 and 0.7. Despite the differences in the volumetric response, all soil samples collapse once wetted. However, in the soil samples with the as-compacted void ratio lower than 0.5, the swelling due to stress unloading is more pronounced than the compression caused by volumetric collapse. This explains the increase in volume observed when the final

stationary conditions are achieved. Globally the model predicts fairly well the after imbibition void ratio over the entire range of void ratio and vertical stress tested.

Analysis of the numerical results

Model validation

The main results of Test 1 are compared with the data to verify the ability of the MCCM to correctly reproduce wetting-induced deformations.

Time evolution of the predicted crest settlements are shown in Fig. 6, together with the measurements read by LVDT and laser transducers obtained by Thorel *et al.* (2011). The numerical results refer to two nodes, N1 and N2, located at the crest embankment along the axis and the slope (see Fig.4). The comparison between model predictions and experimental data is quite satisfactory. The major differences are observed in Phase 1 when the centrifuge acceleration is applied to the embankment scale model (see Fig. 6a). In this phase, the measured vertical displacements increase up to stationary values ranging from 0.6 to 2.4 mm. The predicted settlements develop quicker and vary within a thinner range (1.6-2.1 mm) with respect to what is experimentally observed.

Figure 6b illustrates the time evolution of the crest vertical displacements induced by the imbibition process. Zero values correspond to the settlements registered at the end of the in-flight phase. In Phase 2, when the water table is imposed at the bottom, no significant difference is observed between the readings of LVDT and laser transducers. Conversely, the model predicts slightly greater settlements near the slope than the axis. In Phase 3, when the second inundation event is simulated, more extensive vertical displacements are registered at the crest slope than the axis. This feature is well reproduced by the MCCM and is due to the lateral displacements that develop during the imbibition process.

The spatial distributions of the vertical displacements and void ratio e are depicted in Fig. 7. The numerical results refer to a vertical axis 0.5 cm far from the axis of symmetry and are compared with the experimental data. The predicted settlements increase in magnitude as the water table moves upwards from the bottom to 5 cm above the embankment base (see Fig. 7a). The settlement profiles have similar trends in Phases 2 and 3. In the lower part, the stress unloading is accompanied by an increase of the vertical displacements due to appreciable positive vertical strains. Conversely, in the upper part, the SCM behaves as an elastic material and no marked change in the magnitude of settlements is observed. These results are consistent with the measurements and point out that the capillary rise causes the triggering of the so-called volumetric collapse in the deep layers. This phenomenon occurs in both phases but it is more pronounced in the second, when saturated conditions are achieved in the lower part of the embankment.

Void ratio profiles are reported in Fig. 7b. The experimental data are calculated from the vertical displacements by assuming oedometric boundary conditions. The increase of S_r is accompanied by a progressive reduction in volume in the lower part of the embankment and elastic swelling in the upper part. The model slightly overestimates the wetting-induced deformations in Phase 2 while it accurately describes the experimental data in Phase 3.

Based on the comparisons shown in this section, it can be concluded that the model can well reproduce the embankment response to inundation events.

Hydro-mechanical response of the embankment during inundation

Once the accuracy of the numerical results is verified, the hydro-mechanical behavior of the embankment is analyzed focusing attention mainly on the spatial-temporal evolution

of pore-water pressure u , saturation degree and total vertical stress, as well as, the stress paths and the displacement fields.

Spatial-temporal evolutions of u , S_r and σ_v are plotted in Fig. 8 with reference to two vertical axes 5 and 28.5 cm far from the axis of symmetry. This means that the second vertical axis passes through the crest slope. The thick lines identify the u , S_r and σ_v distributions during the main phases of the test, in detail: lines 0 refer to the initial conditions; lines 1 define the profiles at the end of the in-flight phase; lines 2 represent the distributions once concluded Phase 2 and, finally, lines 3 identify the profiles on attaining the stationary conditions in Phase 3. The thin lines represent the u , S_r and σ_v profiles with depth at certain times ($t=1.83$ h, 4.86 h) during equalization process. The reference points A, B, C, D, E and F refer to an element located at the depth z of 10.75 cm close to the axis of symmetry.

Because of the imposed hydraulic boundary conditions, u profiles are not dependent on distance from the symmetry axis. Indeed, the pore-water pressure distributions along the two considered vertical axes are completely coincident (see Fig. 8a). As the g level increases, u profiles rotate in a counterclockwise direction, keeping a constant value at a depth of 7 cm (line 1). The position of the centre of rotation is controlled by the initial conditions and the WRC, while the slope of the curve is imposed by the gravitational acceleration. When the water table is kept at the base of the SCM layer, a water flow takes place over the embankment body and the pore-water pressures progressively increase up to hydrostatic stationary values (line 2). During the second inundation event, water infiltrates from the slope and the sand-embankment interface level and the water table moves upwards from the bottom up to a distance of 5 cm. The pore-water pressures increase again and hydrostatic conditions are gradually achieved (line 3).

The S_r profiles are reported in Fig. 8b. The increase of the gravitational acceleration induces no appreciable change in saturation degree profile. This is mainly due to the

initial conditions, in terms of S_r and s , and the shape of the WRC. The point representative for the initial conditions lies on the vertical branch of the WRC, along which large variations of pore-water pressure are accompanied by negligible variations of the degree of saturation. In Phase 2, as the water progressively rises up through the embankment, saturation degree increases. The increment of S_r , ΔS_r , varies in magnitude depending on the position of the considered element. Indeed, the same variation of the pore-water pressure entails more extensive ΔS_r in the deep than in the shallow elements. This results from the differences in suction level reached upon ending the in-flight phase, as well as the shape of the WRC. In Phase 3, S_r increases again and saturated conditions are achieved below the current position of the water table. Analogously to the u profiles, the evolution of S_r is not influenced by the position of the considered vertical axis. Indeed, there is no difference between the S_r profiles near the axis of symmetry and the slope. Obviously this outcome is strictly connected to the simple WRC model adopted in this study. Using more advanced retention models (that incorporate the dependence on the current void ratio), S_r profiles could vary depending on the considered vertical axis coherently with the different volume changes predicted near the slope and the axis .

Consider now the σ_v profiles depicted in Fig. 8c. During the in-flight phase, the slope of the curve abruptly increases according to the increase in the gravity loading exerted on the solid skeleton. In the subsequent phases, the small variations in the σ_v profile stem from the changes in the unit soil weight γ due to the propagation of the wetting front. The comparison between the σ_v profiles relative to the two considered vertical axes reveals that the evolution of σ_v is affected by the distance from the axis of symmetry. Indeed, the variations of σ_v in the vicinity of the slope are less pronounced than those observed near the axis.

The analysis of the u , S_r and σ_v profiles provide also information about the changes in the effective vertical stresses σ_v' . In Phase 1, the increase of the gravity loading entails an increase of σ_v' that is more pronounced in the deep layers far from the slope. In Phases 2 and 3, the evolution of σ_v' is mainly governed by the changes in suction level. In both phases σ_v' decreases and its reduction is larger in the lower part of the embankment than in the upper and, at a given depth, is greater in Phase 2 compared with Phase 3.

A better understanding of the wetting-induced stress changes can be gained through the analysis of the stress paths followed by two elements, EL1 and EL2, located at the same depth ($z=10.75$ cm) close to the axis and the slope, respectively (see Fig. 4).

The stress path of the element EL1 is represented in the (p', q) plane, emphasizing the relative position of the current stress state with respect to the current yield surface (see Fig. 9a). The evolution of the specific volume is plotted in the (p', v) plane, together with the NCLs relative to the current saturation degree and the initial URL (see Fig. 9b).

The initial stress state of the EL1 lies inside the yield surface, as expected for over-consolidated soils. In oedometric conditions, the increase of the gravitational acceleration forces the stress state to move towards the K_θ -line (branch AB). The response in the compressibility plane is initially controlled by the slope of the URL and then by the slope of the NCL related to the current saturation degree. Modifying the hydraulic boundary conditions at the bottom, a capillary front starts to rise up within the soil layer. As the front propagates below the considered element, the stress ratio η , defined as ratio between q and p' , increases even if no appreciable change in the pore-water pressure and the saturation degree is observed (branch BC). When the capillary front passes through the EL1 and propagates upwards, the pore-water pressure and the saturation degree progressively increase. Although both stress invariants decrease, the

shrinkage of the yield surface constantly keeps the current stress state in elastic-plastic regime (branch CD). Consequently, the stress path tends again towards the K_0 -line and the volumetric collapse occurs. The evolution of the stress state imposed by the second inundation is definitely similar to that just described. As the water infiltrates from the bottom and the slope, the stress ratio in the considered element increases (branch DE). When the front reaches EL1, the saturation degree increases, the elastic domain shrinks and the stress state is forced to lie again on the current yield surface (branch EF). Similarly to what is observed in Phase 2, the stress path tends to the K_0 -line and the evolution of the stress state is accompanied by negative variations of the specific volume.

Let us now consider the element EL2 located just below the slope at the same depth as EL1. The responses in the (p', q) and (p', v) plane are analyzed emphasizing the main differences with respect to those of EL1 (see Fig. 10).

The initial stress state is practically coincident with that of EL1, because at 1 g the suction level and saturation degree keep constant values within the entire embankment. The application of the centrifuge acceleration entails an increment of the gravity loading exerted on the solid skeleton. As the distance between EL2 and the slope is narrow, the variation of σ_v is significantly lower than that observed in the EL1 and is insufficient to lead the current stress state on the yield surface (branch AB). The soil response in the compressibility plane is, hence, controlled by the slope of the URL. When null pore water pressure is prescribed at the embankment base, the mean effective stress decreases and the saturation degree increases. Consequently, the stress path points towards the origin of the p' -axis and the current yield surface shrinks. As long as the stress state moves within the ellipse, the soil response is elastic and the volumetric behavior obeys the URL. When the ellipse captures the stress state, the stress path abruptly changes in slope and the soil response in the compressibility plane deviates

from the URL (last part of the branch CD). The elastic swelling induced by stress release is partially balanced by the plastic strains caused by volumetric collapse. Therefore, the solid skeleton swells again but the amount of the increase in volume is lower than that predicted assuming an elastic response of the material. Finally, the soil response to the second inundation event is similar to that described above (branch DF). The pronounced shrinkage of the ellipse keeps the stress state in elastic-plastic regime and the solid skeleton swells again.

The analysis of the numerical results reported in Figs. 9-10 highlights how the hydro-mechanical response of the soil elements depends on their position within the embankment body. The stress path of the EL1 obeys the K_0 -line and is qualitatively similar to that followed by all deep elements located near the axis. Instead, the stress path of the EL2, that is representative for the wetting-induced stress changes in the elements placed in the upper part or near the slope, approaches the critical state line. Moreover, the last finding demonstrates the importance of monitoring soil behavior near the slope, where potentially unstable conditions could occur. Similar outcomes were obtained by Laloui *et al.* (2015) when studying the hydro-mechanical behavior of a volcanic ash slope during rainfall. Despite the fact that the geometry of the soil domain and the wetting path are very different, the Authors found that the direction of the stress paths varies with the depth of the considered elements, but that all stress paths move towards the critical state line.

The displacement fields induced by total stress changes (Phase 1) and suction losses (Phases 2 and 3) are plotted in Fig. 11 in terms of ratio C between the variations of horizontal and vertical displacements in each phase, $C = \Delta\delta_h / \Delta\delta_v$. Here, pale grey indicates the soil region where plastic volumetric strains occur. During the in-flight phase, the increase of the gravity loading produces irreversible volume changes only where the embankment is deepest (see Fig. 11a). The thickness of the grey zone

decreases when approaching the slope and is null at a distance of approximately 45 cm from the axis of symmetry. This result is consistent with the spatial distribution of the total vertical stress shown in Fig. 8c. The increase of the total stresses is more pronounced in the lower part of the embankment near the axis of symmetry. Consequently, the magnitude of crest settlements is larger near the axis than the slope (see Fig. 6a). The increase of the g -level generates also horizontal displacements δ_h (see C contours). These displacements primarily occur near the slope and are negligible for d lower than the crest length L_{top} . During the first inundation event, volumetric collapse phenomena are observed in the lower part of the embankment (see Fig. 11b). The grey area extends up to the slope with thickness ranging from 7.0 to 14.0 cm. Differently from Phase 1, no noticeable change in the thickness of the plastic region is observed for d lower than L_{top} . This is coherent with the variations of u and S_r that keep constant values in the entire embankment. As a consequence, there is no significant difference between the increase of δ_v measured by LVDT and laser transducers (see Fig. 6b). Together with the vertical displacements, the suction losses cause the occurrence of horizontal displacements. The ratio C increases in magnitude approaching the slope and reaches maximum values in the vicinity of the embankment toe. This distribution indicates that the reduction in lateral confining stress emphasizes the horizontal displacements. In the last phase, the inundation event leads to the development of plastic volumetric strains through much of the embankment body (see Fig. 11c). Analogously to Phase 2, the plastic region shows no appreciable change in thickness below the embankment crest. However, differently from the previous phase, the settlements registered near the slope are larger than those measured near the axis. This difference between Phases 2 and 3 can be explained by analyzing the C contours. Focus the attention, for example, on the vertical axis passing through the crest slope: C ranges from 0.4 (in the upper part) to 0.6 (in the lower part) in the Phase 2 and from 0.3 to 0.8

in the Phase 3. This means that the second inundation event generates more extensive horizontal displacements than the first one. This result is found also by comparing the original (thin dashed line) and deformed (thin continuous line) embankment geometries in the two considered phases. The development of these displacements emphasizes the settlements and is responsible for the differences in the magnitude of δ_v observed in Fig. 6.

Influence of the as-compacted conditions on the embankment response

The impact of the as-compacted conditions on the hydro-mechanical behavior of the embankment is evaluated by performing two additional numerical analyses. The values for γ_d and w , adopted in the analyses, range from 82 to 100% of γ_{MDD} and from 10.5 to 13.5%, respectively (see Fig. 12). In the reference analysis (Test 1) the soil is compacted in loose conditions, which are poorly representative of actual field conditions. In Tests 2 and 3, the after-compaction conditions satisfy recommendations for the construction of roadway embankments that require that the sub-layers are compacted to a density of at least 90-95% of γ_{MDD} , verifying that the moisture content can attain the specified density.

The numerical results are compared in Fig. 13 in terms of time evolution of crest vertical displacements at the axis and the crest slope. The magnitude of the vertical displacements appreciably decreases as the dry density increases. In particular, when the sub-layers are compacted at γ_{MDD} (Test 3), the embankment elastically swells and the vertical displacements are totally negligible. The improvement of the compaction procedure also modifies the horizontal displacement field. The latter decreases in magnitude as γ_d increases, as reveals the reduction in the difference between the crest displacements at the axis and the slope.

These results confirm that the wetting-induced behavior of the compacted soil is deeply affected by the after-compaction conditions. Optimizing the compaction procedure, the saturation degree increases, as well as the Over Consolidation Ratio (OCR). Obviously, this leads to a reduction of the S_r variation due to inundation and an increase of the distance between the initial stress state and the yield surface. Both factors minimize the risk that the soil response results "in collapsing".

Figure 14 shows the spatial distribution of the plastic volumetric strains ε_v^p in Test 1 at the end of simulation. The plastic volumetric deformations increase in magnitude proceeding downwards from the crest to the bottom. The irreversible volume changes keep within 1.0% in the upper part and reach the maximum values in the saturated zone close to the axis of symmetry. The strain rate considerably increases approaching the position of the water table, as demonstrated by the reduction in the distance between contour lines.

Figure 15 depicts the spatial distribution of ε_v^p in Test 2, once the final stationary conditions are reached. It can be noted that there are some similarities between the ε_v^p patterns shown in Figs. 14-15. In both cases, the extent of the plastic volumetric strains distinctly depends on the relative position with respect to the crest and the axis; moreover, the distance between the ε_v^p contours decreases approaching the water table. However, there are significant quantitative differences in the two analyzed cases: in the first the maximum volume change exceeds 16% while in the second it keeps within 10%. This explains the differences underlined above regarding the amount of the crest vertical displacements (e.g. Escario and Saez 1973; Lawton *et al.* 1989; Muñoz-Castelblanco *et al.* 2011; Vilar and Rodrigues 2011; Casini *et al.* 2012).

Conclusions

This study analyzes the embankment response to inundation using a hydro-mechanical model formulated in terms of Bishop's effective stress and suction and implemented in the commercial code Abaqus/Standard. The study has been performed by means of a two-dimensional finite element model that accurately reproduces the geometry and the sequence of steps of the centrifuge test conducted by Thorel *et al.* (2011). The mechanical response of the soil behavior is modeled by adopting the Modified Cam-Clay constitutive model extended to the case of partially saturated soils. The water retention curve is described by the Van Genuchten equation and the relative permeability is expressed as a power function of the degree of saturation. The comparison between the predictions and the experimental data demonstrates the ability of the MCCM to reproduce the wetting-induced displacement field at a different scale from laboratory tests to the physical model. Besides providing a validation of the model, the study highlights the importance of the hydraulic soil properties, the external perturbation and the as-compacted conditions for the triggering of the volumetric collapse.

In particular, from the analysis of the numerical results, it has been found that:

- the wetting-induced settlements can be roughly predicted on the basis of 1D compression tests, as suggested by Thorel *et al.* (2011). The small difference between the crest settlements near the axis and the slope (about 10%) is consistent with the variations of the effective stresses and strains associated with the suction losses within the embankment;
- the difference in crest settlements for increasing values of distance stems from the reduction of the lateral confining stress exerted on the solid skeleton.

Because of this, the same perturbation generates more extensive positive vertical deformations, due to volumetric collapse phenomena, near the slope;

- the stress paths and the volumetric behavior depend on the position of the elements considered. Although failure conditions never occur in the analyzed cases, the study emphasizes that particular attention should be paid to the monitoring of the soil behavior near the slope surface;
- the magnitude of the wetting-induced settlements can be reduced by improving the compaction procedure. It is clear that the relevance of volumetric collapse phenomena progressively reduces as dry density increases. Such phenomena never occur when the soil layers are compacted at the maximum dry density.

References

- Alonso, E.E., Gens, A., and Josa, A. 1990. A constitutive model for partially saturated soils. *Géotechnique*, **40**(3): 405–430.
- Casini, F. 2012. Deformation induced by wetting: a simple model. *Canadian Geotechnical Journal*, **49**(8): 954-960.
- Casini, F., Vaunat J., Romero E. and Desideri, A. 2012. Consequences on water retention properties of double-porosity features in a compacted silt. *Acta Geotechnica*, **7**(2): 139–150.
- Cafaro, F., Hoffmann, C., Cotecchia, F., Buscemi, A., Bottiglieri, O., and Tarantino, A. 2008. Modellazione del comportamento idraulico di terreni parzialmente saturi a grana media e grossa. *Rivista Italiana di Geotecnica*, **3**: 54-72.
- Durgunoglu, H.T., and Mitchell, J.K. 1975. Static penetration resistance of soils, I - Analyses. Proceedings of the Conference on in situ measurement of soil properties, ASCE, New York, 151-171.
- Escario, V., and Saez, J. 1973. Gradual collapse of soils originated by a suction decrease. *In* Proceedings of 8th International Conference on Soil Mechanics and Foundation Engineering, Moscow, 6–11 August 1973. USSR National Society for Soil Mechanics and Foundation Engineering, **4.2**: 123-124.
- Ferber, V., Auriol, J.C., Cui, Y.J., and Magnan, J.P. 2008. Wetting-induced volume changes in compacted silty clays and high-plasticity clays. *Canadian Geotechnical Journal*, **45**(2): 252–265.
- Gens, A., Alonso, E.E., and Suriol, J. 1995. Effect of structure on the volumetric behaviour of a compacted soil. In 1st International Conference on Unsaturated Soils, UNSAT1995. *Edited by* Alonso and Delage. A.A. Balkema, Rotterdam, 83–88.
- Gens, A., Sánchez, M., and Sheng, D. 2006. On constitutive modelling of unsaturated soils. *Acta Geotechnica*, **1**(3): 137–147.

Jommi, C. 2000. Remarks on the constitutive modelling of unsaturated soils. In *Experimental Evidence and Theoretical Approaches in Unsaturated Soils. Proceedings of the International Workshop on Unsaturated Soils, Trento. Edited by A. Tarantino and C. Mancuso.* Balkema, Rotterdam. 139–153.

Jommi, C., and di Prisco, C. 1994. A simple theoretical approach for modelling the mechanical behaviour of unsaturated soils. In *Italian Conference, Il ruolo dei fluidi nei problemi di ingegneria geotecnica, Mondovi*, 167–188.

Kimura, T., Kusakabe, O., and Saitoh, K. 1985. Geotechnical model tests of bearing capacity problems in a centrifuge. *Géotechnique*, **35**(1), 33–45.

Laloui, L., Ferrari, A., Li, C., and Eichenberger, J. 2016. Hydro-mechanical analysis of volcanic ash slopes during rainfall. *Géotechnique* **66**(3): 220–231

Lawton, E.C., Frigaszy, R.J., and Hardcastle, J.H. 1989. Collapse of compacted clayey sand. *Journal of Geotechnical Engineering*, **115**(9): 1252–1267.

Mašín, D. 2010. Predicting the dependency of a degree of saturation on void ratio and suction using effective stress principle for unsaturated soils. *International Journal for Numerical and Analytical Methods in Geomechanics*, **34**: 73–90.

Muñoz-Castelblanco, J., Delage, P., Pereira, J.M., and Cui, Y.J. 2011. Some aspects of the compression and collapse behaviour of an unsaturated natural loess. *Géotechnique Letters*, **1**(2): 17–22.

Nakase, A., Kusakabe, O., and Wong, S. 1984. Centrifuge Model Tests on Bearing Capacity of Clay. *Journal of Geotechnical Engineering*, **110**(12): 1749–1765.

Nuth, M., and Laloui, L. 2008. Advances in modelling hysteretic water retention curve in deformable soils. *Computers and Geotechnics*, **35**(6): 835–844.

Or, D. 1996. Wetting-induced soil structural changes: The theory of liquid phase sintering. *Water Resources Research*, **32**(10): 3041–3049.

Ovesen, N. K. 1975. Centrifugal testing applied to bearing capacity problems of footing on sand. *Géotechnique*, **25**(2): 394–401.

Rodrigues, R.A. 2007. Modelação das deformações for colapso devidas à ascensão de lençol freático. PhD thesis, Escola de Engenharia de São Carlos/USP, São Carlos, Brasil.

Romero, E., and Vaunat, J. 2000. Retention curves in deformable clays. In *Experimental Evidence and Theoretical Approaches in Unsaturated Soils*. Proceedings of the International Workshop on Unsaturated Soils, Trento. *Edited by* A. Tarantino and C. Mancuso. Balkema, Rotterdam, 91–106.

Robertson, P. K., and Campanella, R. G. 1983. Interpretation of cone penetration tests. Part I: Sand. *Canadian Geotechnical Journal*, 1983, **20**(4): 718-733.

Rotisciani, G. M., Sciarra, G., Casini, F., and Desideri, A. 2015. Hydro-mechanical response of collapsible soils under different infiltration events. *International Journal for Numerical and Analytical Methods in Geomechanics*, **39**(11): 1212–1234.

Salager, S., Nuth, M., Ferrari, A., and Laloui, L. 2013. Investigation into water retention behaviour of deformable soils, *Canadian Geotechnical Journal*, **50**(2), 200-208.

Sheng, D., Fredlund, D.G., and Gens, A. 2008. A new modelling approach for unsaturated soils using independent stress variables. *Canadian Geotechnical Journal*, **45**(4): 511–534.

Soranzo, E., Tamagnini, R., and Wu, W. 2015. Face stability of shallow tunnels in partially saturated soil: centrifuge testing and numerical analysis. *Géotechnique*, **65**(6): 454-467

Sun, D.A., Sheng, D., Xiang, L., and Sloan, S.W. 2008. Elastoplastic prediction of hydro-mechanical behaviour of unsaturated soils under undrained conditions. *Computers and Geotechnics*, **35**(6): 845–852.

Tamagnini, R. 2004. An extended Cam-clay model for unsaturated soils with hydraulic hysteresis. *Géotechnique*, **54**(3): 223–228.

Tamagnini, R. 2011. On the effective stress principle in unsaturated soil. *Rivista Italiana di Geotecnica*, **3**: 25-31.

Tarantino, A., and Pozzato, A. 2008. Strumenti per il monitoraggio della zona non satura. *Rivista Italiana di Geotecnica*, **3**: 109–125.

Tarantino, A. 2009. A water retention model for deformable soils. *Géotechnique*, **59**(9): 751–762.

Thomas, H., and He, Y. 1998. Modelling the behaviour of unsaturated soil using an elasto-plastic constitutive model. *Géotechnique*, **48**(5): 589–603.

Thorel, L., Ferber, V., Caicedo, B., and Khokhar, I. 2011. Physical modelling of wetting-induced collapse in embankment base. *Géotechnique*, **61**(5), 409-420.

Vilar, O.M., and Rodrigues, R.A. 2011. Collapse behavior of soil in a Brazilian region affected by a rising water table. *Canadian Geotechnical Journal*, **48**(2), 226–233.

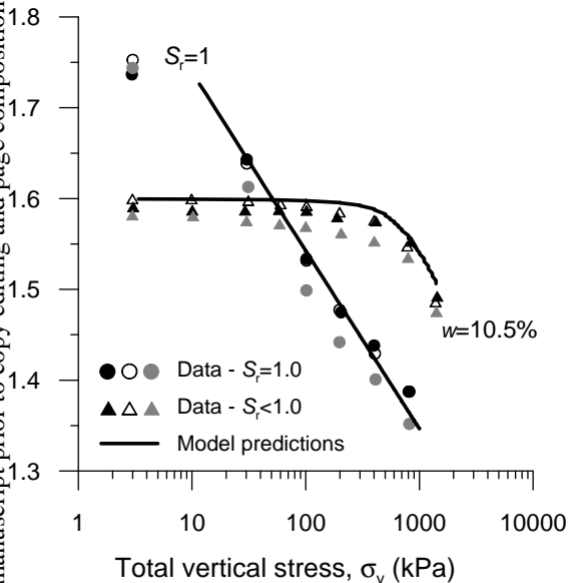
White D. J., Teh K. L., Leung C.F., and Chow Y.K. 2008. A comparison of the bearing capacity of flat and conical circular foundations on sand. *Géotechnique*, **58**(10): 781-792.

Zhou, A., Sheng, D., Sloan, S., and Gens, A. 2012. Interpretation of unsaturated soil behaviour in the stress-saturation space, I: Volume change and water retention behaviour. *Computers and Geotechnics*, **43**, 178-187, 2012.

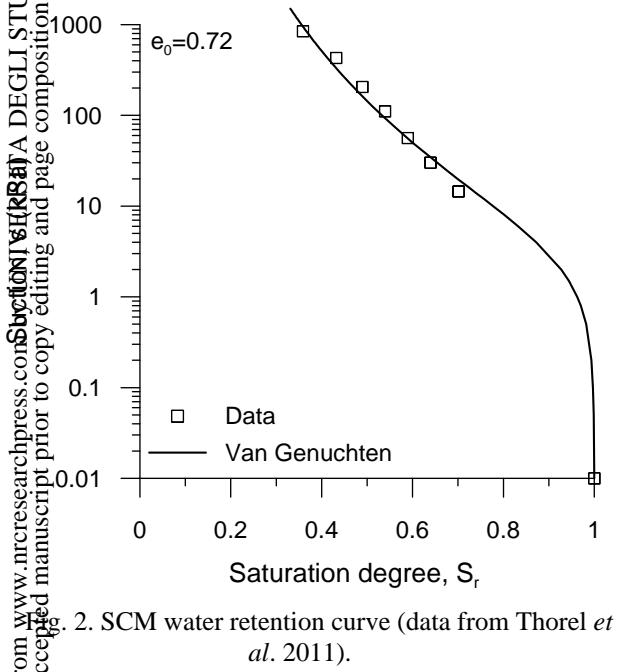
Zhou, A., Sheng, D., Sloan, S., and Gens, A. 2012. Interpretation of unsaturated soil behaviour in the stress-saturation space: II: Constitutive relationships and validations. *Computers and Geotechnics*, **43**, 111-123.

Figure captions

- Fig. 1. Oedometric tests on saturated and unsaturated soil samples (data from Thorel *et al.* 2011).
- Fig. 2. SCM water retention curve (data from Thorel *et al.* 2011).
- Fig. 3. Time evolution of crest vertical displacements (data from Thorel *et al.* 2011).
- Fig. 4. The finite element mesh.
- Fig. 5. Wetting tests under constant vertical load (data from Thorel *et al.* 2011).
- Fig. 6. Comparison between measurements and predictions in terms of time evolution of: a) total displacements; b) settlements due to inundation (data from Thorel *et al.* 2011).
- Fig. 7. Comparison between measurements and predictions in terms of: a) vertical displacements, b) void ratio profiles along a vertical axis 0.5 cm far from the axis (data from Thorel *et al.* 2011).
- Fig. 8. Temporal-spatial evolution of: a) pore water pressure, b) saturation degree, c) total vertical stress during the test (0: initial conditions; 1: in-flight phase; 2: water table at the bottom; 3: water table 5 cm above the base).
- Fig. 9. Responses of the element EL1 ($z=10.75$ cm, $d=0.5$ cm) in: a) stress invariant plane, b) compressibility plane.
- Fig. 10. Responses of the element EL2 ($z=10.75$ cm, $d=43.8$ cm) in: a) stress invariant plane, b) compressibility plane.
- Fig. 11. Spatial distribution of the ratio between the variations of horizontal and vertical displacements in: a) Phase 1; b) Phase 2; c) Phase 3.
- Fig. 12. Numerical analyses.
- Fig. 13. Time evolution of the crest settlements at the axis and the slope.
- Fig. 14. Contours of plastic volumetric strains at the end of the Test 1.
- Fig. 15. Contours of plastic volumetric strains at the end of the Test 2.



1. Oedometric tests on saturated and unsaturated soil samples (data from Thorel *et al.* 2011).



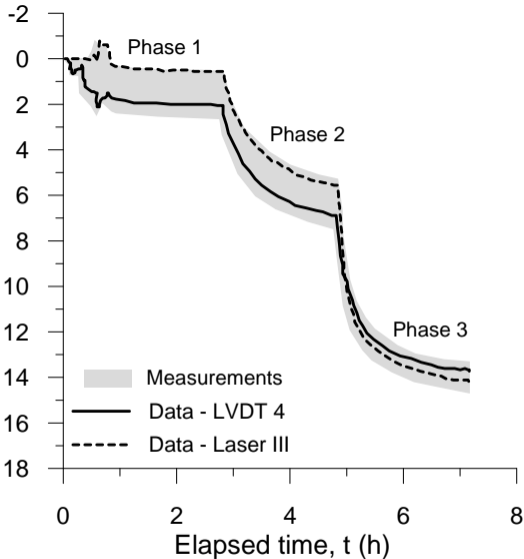


Fig. 3. Time evolution of crest vertical displacements (data from Thorel *et al.* 2011).

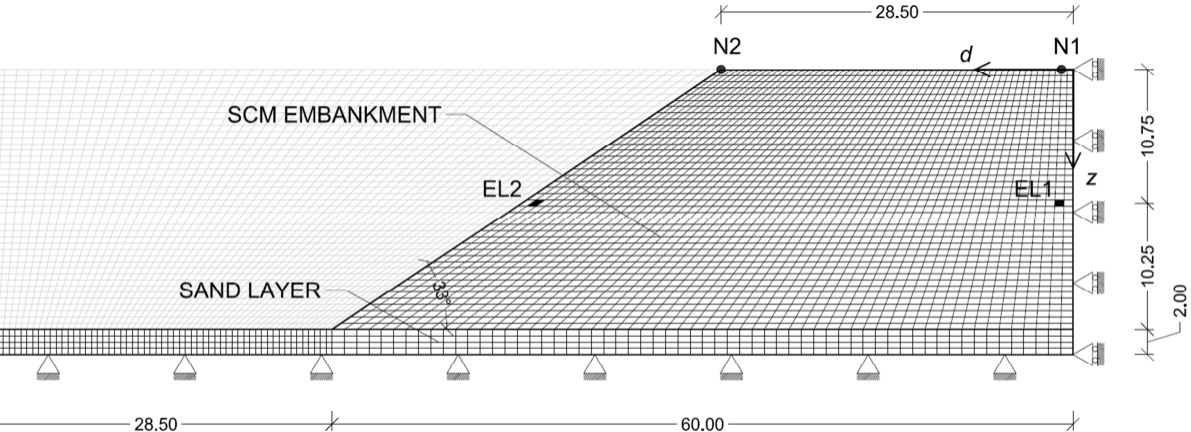


Fig. 4. Wetting tests under constant vertical load (data from Thorel *et al.* 2011)..

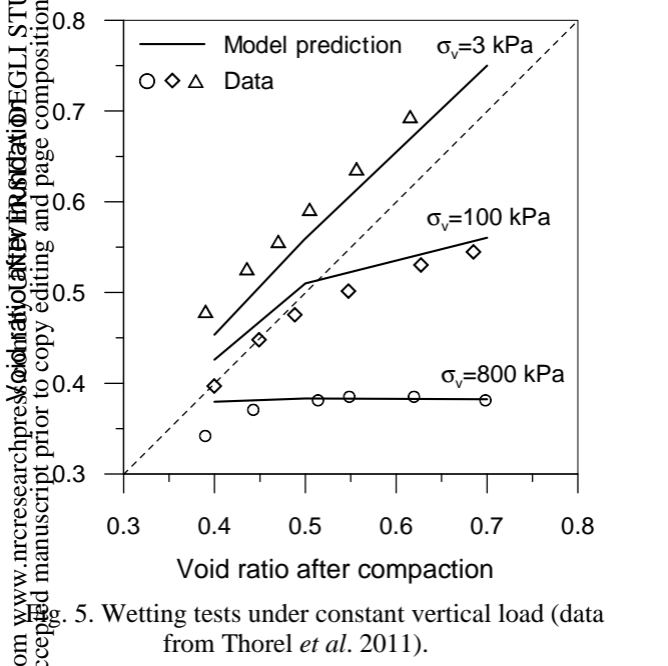
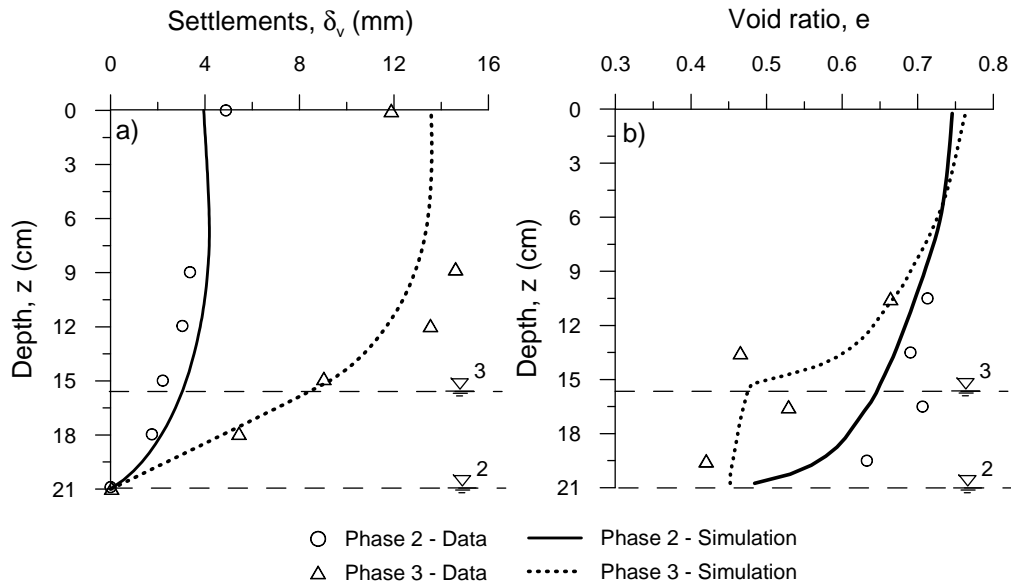
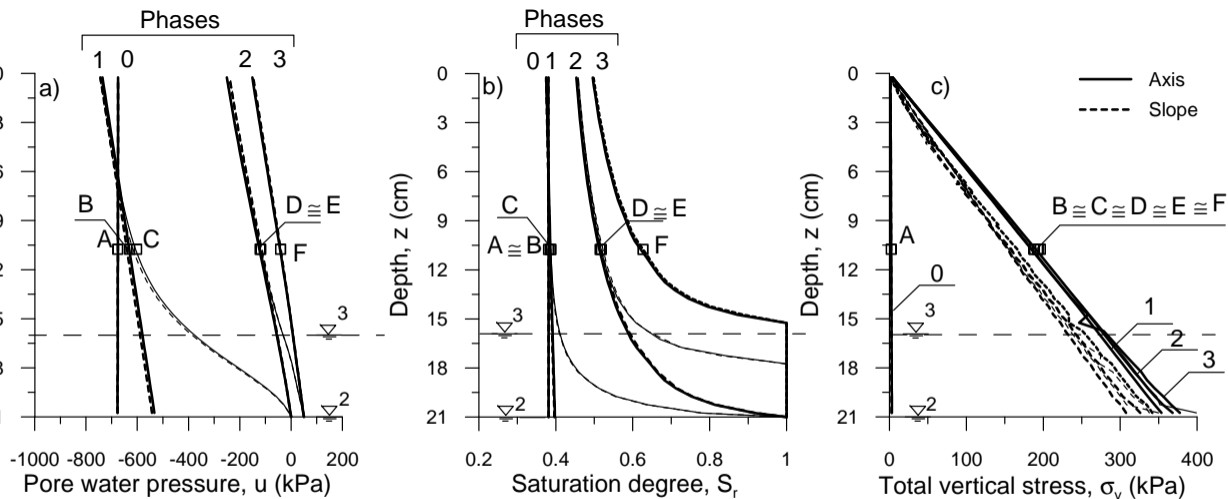


Fig. 5. Wetting tests under constant vertical load (data from Thorel *et al.* 2011).



7. Comparison between measurements and predictions in terms of: a) vertical displacements, b) void ratio profiles along a vertical axis 0.5 cm far from the axis (data from Thorel *et al.* 2011).



8. Temporal-spatial evolution of: a) pore water pressure, b) saturation degree, c) total vertical stress during the test (0: initial conditions; 1: in-flight phase; 2: water table at the bottom; 3: water table 5 cm above the base).

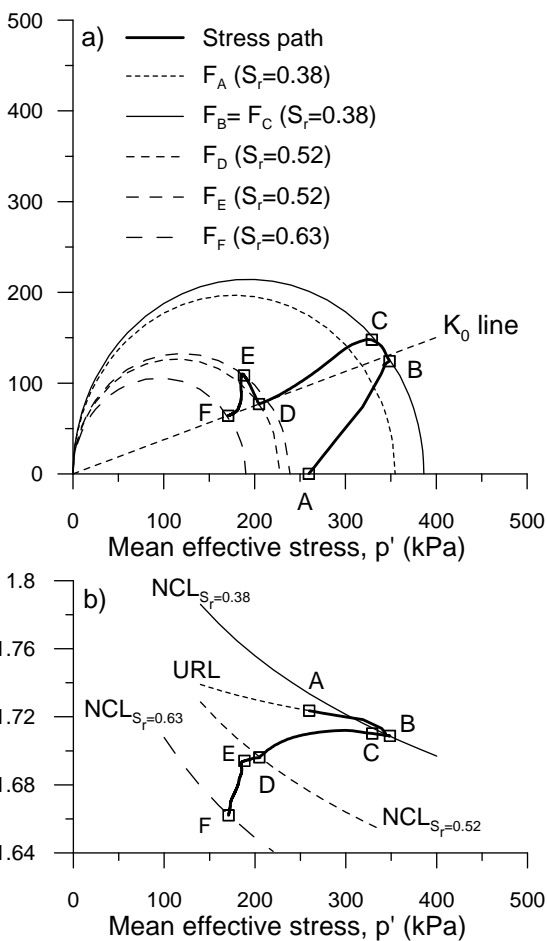
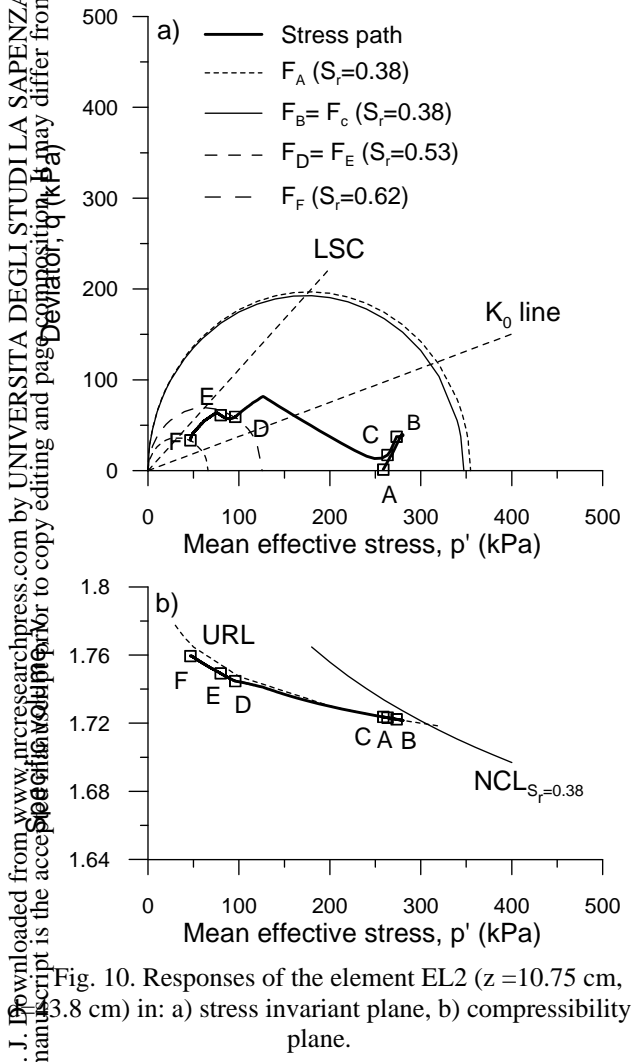


Fig. 9. Responses of the element EL1 ($z=10.75$ cm, 5.5 cm) in: a) stress invariant plane, b) compressibility plane.



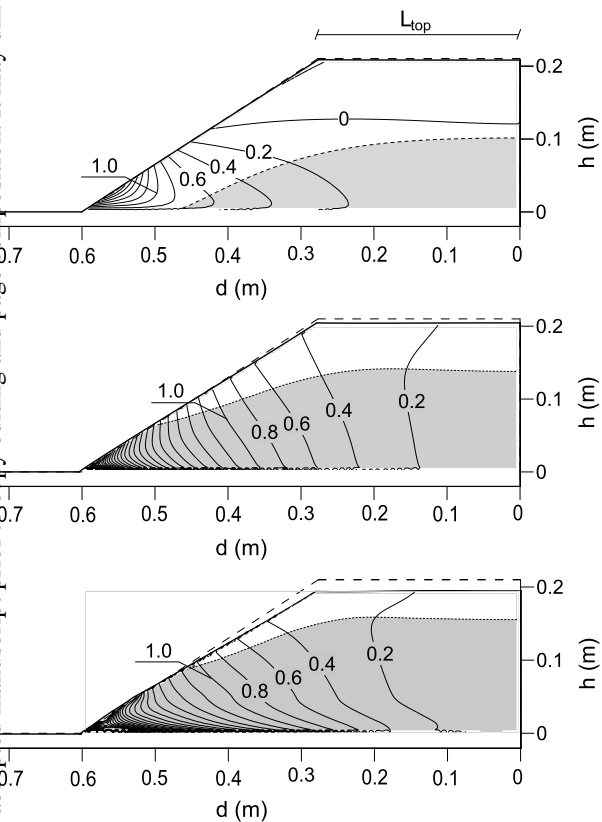
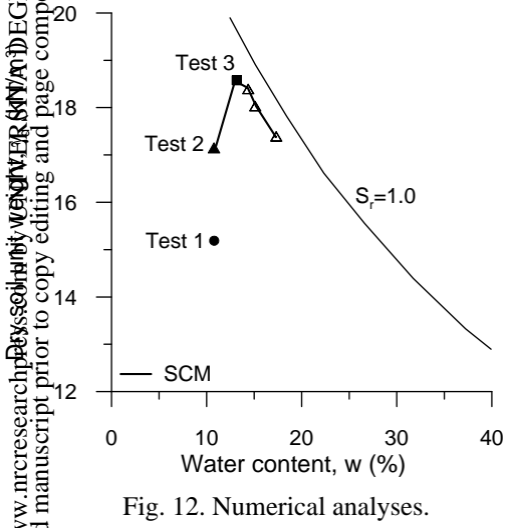


Fig. 11. Spatial distribution of the ratio between the variations of horizontal and vertical displacements in: a) Phase 1; b) Phase 2; c) Phase 3.



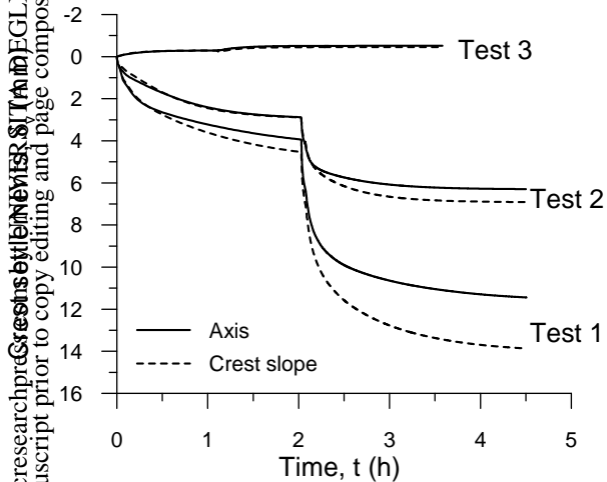


Fig. 13. Time evolution of the crest settlements at the axis and the slope.

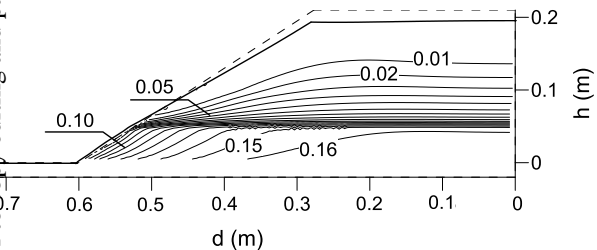


Fig. 14. Contours of plastic volumetric strains at the end of the Test 1.

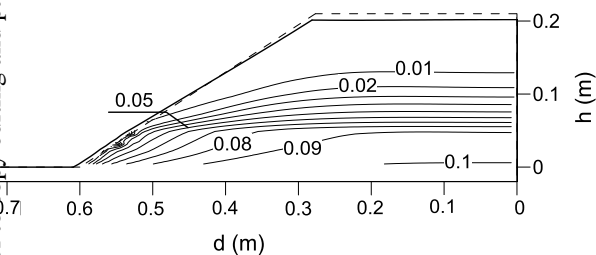


Fig. 15. Contours of plastic volumetric strains at the end of the Test 2.

Tables

Table 1. Numerical analyses.

Test	γ_d (kN/m ³)	w	e_0	S_r
1	15.3	0.104	0.72	0.38
2	16.8	0.104	0.58	0.48
3	18.7	0.135	0.42	0.86

Note: Bold identifies the reference analysis.

Table 2. Constitutive parameters.

	α	$5 \cdot 10^{-5}$
Hydraulic parameters	β	12
	l	1.17
	m	0.15
	k_{sat} (m/s)	$5 \cdot 10^{-8}$
	λ	0.085
	κ	0.025
Mechanical parameters	N_0	1.94
	ν	0.25
	M	1.11
	b	7.4